High-Temperature Grain Size Stabilization of Nanocrystalline Fe-Cr Alloys with Hf Additions

Lulu Li*, Mostafa Saber, Weizong Xu, Yuntian Zhu, Carl C. Koch, Ronald O. Scattergood

Department of Materials Science and Engineering, North Carolina State University, 911 Partners Way, Room 3002, Raleigh, NC 27695-7907, USA

** Corresponding author. Tel.:+1-919-749-5018; fax: +1-919-515-7724. E-mail address: lli18@ncsu.eduu (Lulu Li)*

ABSTRACT

The influence of 1 to 4 at.% Hf additions on the thermal stability of mechanically alloyed nanocrystalline Fe-14Cr alloys was studied in this work. XRD-calculated grain size and microhardness results were reported versus isochronal annealing treatments up to 1100 °C. Microstructural evolution was investigated using channeling contrast FIB imaging and TEM. Grain size of samples with 4 at.% Hf was found to be maintained in the nanoscale range at temperatures up to 1000 °C. Zener pinning was considered as a major source of high temperature grain size stabilization. By comparing the Orowan strengthening contribution to the total hardness, the deviation of grain size predictions from the actual grain size in Fe-14Cr-4Hf suggests the presence of thermodynamic stabilization by the solute segregation to grain boundaries (GBs). A predictive thermodynamic model indicates that the thermodynamic stabilization can be expected.

Keywords: Mechanical alloying; Nanocrystalline Fe-Cr alloys; Grain growth; Thermal stability

Introduction

Nanocrystalline materials possess exceptional physical and mechanical properties due to their nano-scale grains [1]. However, they are usually thermally unstable at high temperatures because of a large driving force for grain growth due to high grain boundary area per unit volume [2].

Kinetic stabilization by solute drag, second-phase particle pinning (Zener pinning) [3], chemical ordering, or porosity can reduce the mobility of grain boundaries (GBs) at high temperatures. The second important mechanism to retain nanocrystalline grain size at high temperatures is thermodynamic stabilization, where a non-equilibrium solute segregates to grain boundaries to reduce the grain boundary energy [4].

Kinetic stabilization occurs, when a moving grain boundary encounters second phase particles. There is a pinning pressure P_z exerting on the grain boundary [5], which reduces mobility. In Zener pinning, $P_z = \frac{3F\gamma}{2r}$ where F, γ and r are the volume fraction, specific GB energy and the radius of the precipitates, respectively. P_z is the pinning pressure on unit area of the boundary . Therefore, stronger pining effect is obtained with a larger volume fraction of smaller precipitates.

In thermodynamic stabilization, the Gibbs interface analysis gives: $\gamma = \gamma_0 + \Gamma_s [\Delta H_{seg} - T\Delta S_{seg}]$ where γ_0 is the non-segregated (intrinsic) grain boundary Gibbs free energy; Γ_s is the solute excess of the grain boundary and $[\Delta H_{seg} - T\Delta S_{seg}]$ is the Gibbs free energy change associated with segregation of the solute atoms into GBs [6, 7]. γ can decrease and reach a metastable equilibrium state with non-equilibrium solute segregating to GBs [6, 8]. In this mechanism, grain growth can be controlled and the nano-scale grain size will be retained at elevated temperatures. The change of grain size versus annealing temperatures was reported by Darling et al. [9] for various solute additions in Fe.

The effect of zirconium additions on grain size stability of mechanically alloyed nanocrystalline Fe-Cr alloys was first reported by Saber et al. [10] and followed by Xu et al.[11]. Hafnium has been used as an addition to titanium, tungsten and iron alloys to improve materials strength at high temperatures, due to second-phase formation [12]. The enthalpy of formation of hafnium oxide is more negative than that of ZrO_2, indicating that the second-phase formation leading to Zener pinning effect might be enhanced in Fe-14Cr-Hf alloy system compared to Fe-14Cr-Zr alloy system [13, 14]. On the basis of our recent models [15, 16], which incorporate elastic strain energies due to atomic size misfits along with chemical contributions for both the primary (base) and secondary solutes, we can evaluate the possible thermodynamic grain size stabilization for nanocrystalline Fe-Cr-Hf alloys.

The objectives of this study were to investigate the effect of hafnium additions on the thermal stability of grain size, and to compare the hafnium additions with zirconium additions with respect to the stabilization mechanisms.

Experimental

Non-equilibrium solid solutions of Fe-14Cr-Hf/Zr containing 0, 2, 4 atomic percent (at. %) of Hf/Zr were synthesized using mechanical alloying in a SPEX SamplePrep 8000M Mixer/Mill. The Fe-14Cr alloy system has no bcc to fcc phase transformation upon annealing treatment which avoids the effect of $\alpha \rightarrow \gamma$ phase transformation on the grain size evolution in this system [17, 18]. Starting materials of pure Fe, Cr, Hf and Zr powders (with 99.9%, 99.9%, 99.995% and 99.95%, respectively) were obtained from Alpha Aesar for ball milling. These starting powders were sealed into a hardened steel vial along with stainless steel balls under argon atmosphere. The ball to powder mass ratio was 10:1. After 20 hours milling, the as-milled powder was

annealed isochronally at different temperatures (from 400°C to 1100°C) for 1 hour under Ar-2%H_2 atmosphere.

X-ray diffraction analyses of the as-milled and annealed samples were carried out using a Rigaku DMax/A X-ray diffractometer using CuK_α radiation with a nominal instrumental broadening of 0.1 °. The grain size was calculated by the Scherrer equation from peak broadening [19] after the subtraction of instrumental broadening, assuming the peaks have the Gaussian profile. The lattice parameter was calculated by Cohen's method combined with the least-square method to minimize error [19, 20]. Vickers hardness was tested for both as-milled and heat-treated powders using a Buehler MicroMet II machine. Powders were mounted on glass slides with Buehler Epothin epoxy. After mechanical polishing, hardness tests were done on individual particles with a load of 50 grams.

Focused ion beam channeling contrast imaging (FIB-CCI) was done on individual particles of Fe-14Cr-4Hf alloys using a FEI Quanta 3D FEG dual-beam FIB system. FIB-CCI images were used to analyze microstructures of the samples in a relatively large area. The transmission electron microscope (TEM) was used to obtain higher resolution images of microstructure for the Fe-14Cr-4Hf alloys annealed at 900 °C. TEM samples were prepared by the FIB "lift-out" technique. TEM images were acquired by a JEM-2010F microscope operating at 200 kV and subsequent image analysis was done using Image J software.

Results and Discussions

Fig. 1a shows the X-ray diffraction patterns of various as-milled Fe-14Cr alloys containing 0-4 at.% Hf/Zr solute additions. The grain size and lattice parameter are also indicated for each composition. As shown in Fig. 1a, there is a peak position shifting toward smaller angles by

adding the solute elements Hf/Zr. This indicates an increase in the lattice constant of Fe-Cr-Hf/Zr alloys. This also shows that a grain size of less than 10 nm is achieved after mechanical alloying via ball milling. Since internal strain exists in the microstructure due to the severe plastic deformation, the calculated grain size from peak broadening can be smaller than the actual grain size. Fig. 1b indicates the changes of the lattice parameters of the bcc alloys versus annealing temperatures. By adding ternary solute elements, lattice parameters of as-milled samples are increased with respect to the reference point (Fe-14Cr). This deviation is attributed to the formation of non-equilibrium solid solution of Fe-Cr alloys with large atomic size misfit caused by- Hf or Zr additions. The higher content of solute added, the more deviation from the reference point occurs. It is evident that excess solute is dissolved into the solid solution of as-milled samples. The trend in Fig. 1b is similar for different alloy compositions: lattice parameters decrease as T is increased. This indicates that excess solute atoms and vacancies gradually come out of solid solution. Above 700 °C, all the lattice parameters converge to the same value, within experimental error. The similar lattice parameters of samples annealed at higher temperatures implies that excess solute atoms are no longer present within the bcc matrix.

Fig. 2a and 2b show the XRD grain size and Vickers hardness, respectively, of various alloys as a function of annealing temperatures. Since lattice strain broadening caused by the presence of second phases is not included in the Scherrer's method, the actual grain size of annealed samples can be significantly larger than the value calculated from the XRD pattern [10]. Based on prior experiences, we assume alloys to be nanocrystalline only if the XRD value is less than 40 nm. It is necessary to confirm the grain size by the use of FIB channeling contrast or TEM images.

At lower annealing temperatures (0 to 400 °C), the Vickers hardness of each alloy is high ($\geq$ 8 GPa) due to the defects introduced during the ball milling [21] and the nanocrystalline grain size.

The hardness slightly increased up to 400 °C while there is no significant increase in the grain size. The unrelaxed atomic structure and high dislocation density, introduces excess enthalpy into the as-milled microstructure [22]. At low temperature annealing, the excess enthalpy is released through relaxation of large angle grain boundaries without significant grain growth. The grain boundaries reconstruct to a more continuous and ordered state [23] with grain boundary dislocations regularly spaced, enhancing the mechanical properties. Excess vacancies generated during ball milling also facilitate solute atom diffusion to the dislocations [24, 25], and contribute to dislocation pinning. This leads to a hardness increase at low temperature annealing up to 400 °C. In this range of temperature, there is no difference in the effect of Hf and Zr additions on the microstructural evolution and hardness change. Since the diffusion rate of Hf/Zr is very slow in this temperature range, the solute drag mechanism would be the most effective mechanism to mitigate grain growth [2, 26-28].

At intermediate annealing temperatures (400 °C to 800 °C), the XRD grain size of Fe-14Cr base alloy is increased beyond the nano-scale range (Fig. 2a). This is consistent with the hardness evolution which sharply drops with increasing annealing temperatures (Fig. 2b). By adding solute atoms of Hf/Zr, the grain size remains in the nano-scale range up to 800 °C (Fig. 2a), and the hardness decreases more gradually compared to the alloy with no Hf/Zr additions (Fig. 2b). In this range of temperature, the XRD results show only bcc peaks and no extra peaks corresponding to precipitates are observed. Based on the phase diagrams of Fe-Zr and Fe-Hf alloys [29], the solubility limit for Hf or Zr in Fe is very small, indicating that the fraction of excess solute atoms segregated into GBs could provide thermodynamic stabilization [30], in addition to the solute drag mechanism. The effect of Hf additions on the grain growth and mechanical behavior are similar with Zr additions in this temperature range.

Grain size and hardness at high annealing temperatures (>800 °C) are influenced by both the atomic fraction and the type of the solute additions of Hf/Zr. As shown in Fig. 2a and 2b, increasing the solute content (from 0 to 4 at.%) leads to greater grain size stabilization effect. Both 4 at.% Hf and 4 at.% Zr can stabilize nanocrystalline alloys up to 1000 °C. These alloys still maintain Vickers hardness of 5.2 GPa, which can be useful for high temperature applications. Adding the same content of Hf or Zr addition, the alloy with Hf additions provides better grain size stabilization effect compared to Zr. Hf additions also provide higher hardness than Zr additions up to higher temperature. This is illustrated in Fig. 2b where the hardness of Fe-14Cr-4Hf is higher than that of Fe-14Cr-4Zr after 1000 °C heat treatment.

Fig. 3 shows XRD patterns of four alloys of Fe-14Cr-Hf/Zr annealed at 900 °C. Black arrows indicate extra peaks, which are associated with precipitates. No extra peaks are resolved in the 900 °C annealed Fe-14Cr-2Zr sample. The intensity and the number of extra peaks in Fe-14Cr-4Hf sample are greater than those of Fe-14Cr-4Zr alloy. Additionally, the alloy systems with higher contents of solute addition have more extra peaks than those with lower solute addition. This suggests that Hf additions introduce more precipitates as well as greater stability compared to equivalent amount of Zr. Therefore, the stability of Fe-14Cr-4Hf extends to higher temperatures, compared to the Fe-14Cr-4Zr alloys.

The channeling contrast images of Fe-14Cr-4Hf alloy annealed at 900 °C, 1000 °C， and 1100 °C are shown in Figs. 4a, 4b, and 4c, respectively. Grain size distribution is uniform for each annealing temperature and no abnormal grain growth is observed. The grain size is in the nanoscale range at 900 °C. At 1100 °C, the grains maintained a size of around 200 nm, thus showing excellent high temperature stabilization by Hf solute additions. Fig. 4 also shows that, at annealing temperatures higher than 900 °C, the calculated values for the grain size from XRD

results are no longer reliable because the contribution of precipitation-induced strain to the peak broadening can be significant.

Bright and dark field images and the diffraction pattern are shown in Fig. 5a to 5c for Fe-14Cr-4Hf annealed at 900 °C. The grain size distribution obtained is in the nano-scale range. The diffraction pattern in Fig. 5c shows numerous small spots in-between bcc rings of the matrix, corresponding to the presence of precipitates formed during the annealing treatment. The number average grain size for the distribution (Fig. 5e) is 52 nm, calculated from more than 200 grains measured using the DF images. Moreover, as illustrated in Fig. 5d, the arrows in the enlarged area indicate nanosized precipitates, uniformly distributed throughout the grains. The presence of precipitates is consistent with the extra peaks found in the x-ray diffraction patterns in Fig. 3. Therefore, it is likely that Zener pinning contributes to stabilization of Fe-14Cr-4Hf alloy at high temperatures.

There are several mechanisms contributing to the total hardness of alloys. Grain size refinement can be inferred by the Hall-Petch equation; $\sigma_y = \sigma_0 + K_y D^{-1/2}$; where σ_y is the yield stress, K_y is a constant determined by the slope of the Hall-Petch line, and D is the grain diameter. Since Vickers hardness is related to the yield stress by the relation of $H/\sigma \approx 3$, the Hall-Petch equation can also be given in terms of the hardness [31]: $H_y = H_0 + K_H D^{-1/2}$. The TEM results obtained for mean grain size were 52 nm, 143 nm, and 173 nm for alloys annealed at 900 °C, 1000 °C, and 1100 °C, respectively. The corresponding Hall-Petch plot is shown in Fig. 6. The line plotted includes the base Fe-Cr alloy from ref. [10] and Fe-14Cr-4Hf alloy annealed at 700 °C and 1100 °C. We assume that 700 ° C annealed sample does not form precipitate at this temperature, and also all excess solute Hf atom are segregated to GBs. Therefore, precipitation

and solid solution hardening can be negligible for this sample. At 1100 °C， according to Fig. 4c, grain size increased three times compared to 700 °C. The Orowan strengthening can also be neglected at this point due to coarsening of nano-scale precipitates. Thus, the Orowan strengthening is only considered for the 900 °C and 1000 °C annealed samples. The trend line shown gives H_0=2.31 GPa and K_H=22.35 GPa $nm^{1/2}$. ΔH (Orowan hardening) is calculated through subtraction of the total hardness from the grain size hardening for 900 °C annealed sample. Accordingly, ΔH=1.26 GPa is taken to be the Orowan strengthening contribution (H_{oro}) [32]:

$$\Delta H = H_{oro} = 3\sqrt{3}\left(\frac{\ln(d/r_0)}{\ln(L/r_0)}\right)^{3/2}\frac{Gb}{L}\frac{\ln(L/r_0)}{2\pi}; \quad (1)$$

where d is the precipitate size, L is the interparticle spacing, G is the shear modulus (85.3 GPa), b is the Burgers vector (0.248 nm) and r_0 is the dislocation core radius, assumed to be four times the Burgers vector. Substituting the values of d=23 nm obtained from the TEM images (not shown here) into the Orowan strengthening equation, the interparticle spacing L is obtained as 41 nm. L is related to the volume fraction, f, of spherical particles by:

$$L = d\left[\left(\frac{\pi}{4f}\right)^{\frac{1}{2}} - 1\right]; \quad (2)$$

This predicts that the volume fraction of precipitates is 0.107. According to the Zener pinning model [33]:

$$\frac{D}{d} = \frac{Z}{f^m}\ ; \quad (3)$$

For Fe-based alloys, Z is 1.635 and m=0.5 when f >0.05 [33] and equation (3) gives a grain size of D=115 nm. The deviation of the Zener pinning predictions (115 nm) and the actual grain size

(52 nm) suggests that in addition to kinetic stabilization, there is a possible contribution from thermodynamic stabilization of the nano-grains in Fe-14Cr-4Hf alloy at 900 °C.

To provide insight into the possible thermodynamic contribution, the thermodynamic model by Saber et al. [16] is used to assess the effect of Hf additions on the grain size stability via solute segregation to GBs. Using thermodynamic parameters available in the literature [34-38], the grain size predictions versus the temperature for Hf additions to Fe-14Cr are shown in Fig. 7a. The plot indicates that 4 at.% Hf addition can stabilize the nano-scale grain size up to 1000 °C by the thermodynamic mechanism. However, it should be emphasized that these predictions only consider thermodynamic stabilization in the absence of other contributions. The formation of precipitates can influence the magnitude of solute segregation to GBs, and consequently, the grain size at each annealing temperature would be greater than the value that is predicted by the thermodynamic model. Fig. 7b shows the excess amount of Hf content that would remain in the solid solution at each temperature after segregation to GBs. This indicates that at 900 °C, the Hf content left in the bcc matrix would be sufficient (1.5 at.%) to initiate precipitation, given that the equilibrium Hf solubility in Fe is <1 at.% at 900 °C. Therefore, within this range of temperature, the Zener pinning stabilization would compete with thermodynamic stabilization. HRTEM and EDS-STEM studies are required to establish the contribution of each mechanism to stabilizing nano-scale grain size for this range of temperatures. The characterization of the nanocluster precipitates including crystal structure, chemistry and the orientation relationship to the bcc matrix will be discussed in a forthcoming paper.

Conclusions

This investigation has shown that additions of Hf up to x=4 at.% in ball milled Fe-14Cr-xHf can give effective grain size stabilization in the nano-scale range up to 1000 °C. The hardness of nearly 5.2 GPa is maintained in Fe-14Cr-4Hf at 1000 °C. This offers a possible route for maintaining high strength, thermally stable nanocrystalline ferritic alloys. Employing the Hall-Petch grain size strengthening and Orowan particle strengthening equations for Fe-14Cr-4 at% Hf annealed at 900 °C, the deviation of grain size predictions from the actual grain size suggests the possibility of a thermodynamic stabilization mechanism contribution due to solute segregation to GBs. The use of a thermodynamic model shows that thermodynamic stabilization can be a viable additional mechanism in conjunction with Zener pinning for stabilizing the nano-grains in Fe-14Cr-4Hf at 900 °C.

Acknowledgements

Support for this study by the Department of Energy, Grant DE-NE0000538, is gratefully acknowledged. The authors acknowledge the use of the Analytical Instrumentation Facility (AIF) at North Carolina State University, which is supported by the State of North Carolina and the National Science Foundation.

References

[1] C. Suryanarayana, International Materials Reviews, 40 (1995) 41-64.
[2] C.C. Koch, R.O. Scattergood, K.A. Darling, J.E. Semones, Journal of Materials Science, 43 (2008) 7264-7272.
[3] A. Rollett, F. Humphreys, G.S. Rohrer, M. Hatherly, Recrystallization and related annealing phenomena, Chapter 9, 285-319, Second ed., Elsevier, 2004.
[4] R. Kirchheim, Acta Materialia, 50 (2002) 413-419.
[5] M. Hillert, Acta Metallurgica, 13 (1965) 227-238.
[6] J. Weissmüller, Nanostructured Materials, 3 (1993) 261-272.
[7] J. Weissmüller, Journal of Materials Research, 9 (1994) 4-7.
[8] F. Liu, R. Kirchheim, Scripta Materialia, 51 (2004) 521-525.
[9] K.A. Darling, B.K. VanLeeuwen, C.C. Koch, R.O. Scattergood, Materials Science and Engineering: A, 527 (2010) 3572-3580.

[10] M. Saber, H. Kotan, C.C. Koch, R.O. Scattergood, Materials Science and Engineering: A, 556 (2012) 664-670.
[11] W.Z. Xu, L.L. Li, M. Saber, C.C. Koch, Y.T. Zhu, R.O. Scattergood, Journal of Nuclear Materials, 452 (2014) 434-439.
[12] R.H. Nielsen, G. Wilfing, Hafnium and Hafnium Compounds, Ullmann's Encyclopedia of Industrial Chemistry, Wiley-VCH Verlag GmbH & Co. KGaA, 2000.
[13] G.L. Humphrey, Journal of the American Chemical Society, 75 (1953) 2806-2807.
[14] G.L. Humphrey, Journal of the American Chemical Society, 76 (1954) 978-980.
[15] M. Saber, H. Kotan, C.C. Koch, R.O. Scattergood, Journal of Applied Physics, 113 (2013) -.
[16] M. Saber, H. Kotan, C.C. Koch, R.O. Scattergood, Journal of Applied Physics, 114 (2013) -.
[17] A. Alamo, V. Lambard, X. Averty, M.H. Mathon, Journal of Nuclear Materials, 329–333, Part A (2004) 333-337.
[18] M.A. Auger, T. Leguey, A. Muñoz, M.A. Monge, V. de Castro, P. Fernández, G. Garcés, R. Pareja, Journal of Nuclear Materials, 417 (2011) 213-216.
[19] B.D. Cullity, Elements of X-ray Diffraction, Ch3, 78-103, 1956.
[20] D.L. Dorset, Microscopy and Microanalysis, 4 (1998) 513-515.
[21] R.K. Khatirkar, B.S. Murty, Materials Chemistry and Physics, 123 (2010) 247-253.
[22] C.H. Moelle, H.J. Fecht, Nanostructured Materials, 6 (1995) 421-424.
[23] D. Jang, M. Atzmon, Journal of Applied Physics, 99 (2006) -.
[24] A.A. Nazarov, Interface Science, 8 (2000) 315-322.
[25] H. Kotan, K. Darling, M. Saber, R. Scattergood, C. Koch, Journal of Materials Science, 48 (2013) 8402-8411.
[26] A.W. Bowen, G.M. Leak, Metallurgical Transactions, 1 (1970) 1695-1700.
[27] P. Knauth, A. Charai, P. Gas, Scripta Metallurgica ET Materialia, 28 (1993) 325-330.
[28] A. Michels, C.E. Krill, H. Ehrhardt, R. Birringer, D.T. Wu, Acta Materialia, 47 (1999) 2143-2152.
[29] K. Mahdouk, J.C. Gachon, Journal of Phase Equilibria, 17 (1996) 218-227.
[30] C.C. Koch, R.O. Scattergood, M. Saber, H. Kotan, Journal of Materials Research, 28 (2013) 1785-1791.
[31] X. Liu, M. Nagumo, M. Umemoto, Materials transactions-JIM, 38 (1997) 1033-1039.
[32] D.J. Bacon, U.F. Kocks, R.O. Scattergood, Philosophical Magazine, 28 (1973) 1241-1263.
[33] M. PA, T. Chandra, ISIJ international, 38 (1998) 913-924.
[34] J. Friedel, Advances in Physics, 3 (1954) 446-507.
[35] D.A. Porter, K.E. Easterling, Phase Transformations in Metals and Alloys, (Revised Reprint), CRC press, 1992.
[36] W.R. Tyson, W.A. Miller, Surface Science, 62 (1977) 267-276.
[37] L. Vitos, A.V. Ruban, H.L. Skriver, J. Kollár, Surface Science, 411 (1998) 186-202.
[38] F.R. Boer, R. Boom, W. Mattens, A. Miedema, A. Niessen, (1988).

Figure Captions:

Fig. 1: a) XRD patterns of different alloys under the as-milled condition. D represents diameter of grains, a represents lattice parameter. b) Lattice parameters of each alloy in relation to different annealing temperature.

Fig. 2: a) XRD-calculated grain sizes as a function of annealing temperature and b) Vickers hardness as a function of annealing temperature for different alloy compositions.

Fig. 3: XRD patterns for Fe-14Cr-Hf/Zr alloys annealed at 900°C. Arrows point out extra peaks besides four BCC peaks.

Fig. 4: Channeling contrast FIB image of Fe-14Cr-4Hf alloy annealing at different temperature. a) 900 °C， b）1000 °C，c）1100 °C.

Fig. 5: TEM image of Fe-14Cr-4Hf annealed at 900°C. a) bright field image, b)dark field image, c) diffraction pattern, d) bright field image with higher magnification. The insert image is the enlarged area as plotted in d) of dashed square. e) histogram of number fraction of grain size

Fig. 6: Hall-Petch plot of Fe-14Cr-4Hf alloy along with the base Fe-14Cr alloy.

Fig. 7: Model predictions for Fe-14Cr-xHf alloys. a) grain size b) excess of Hf.

Fig.1

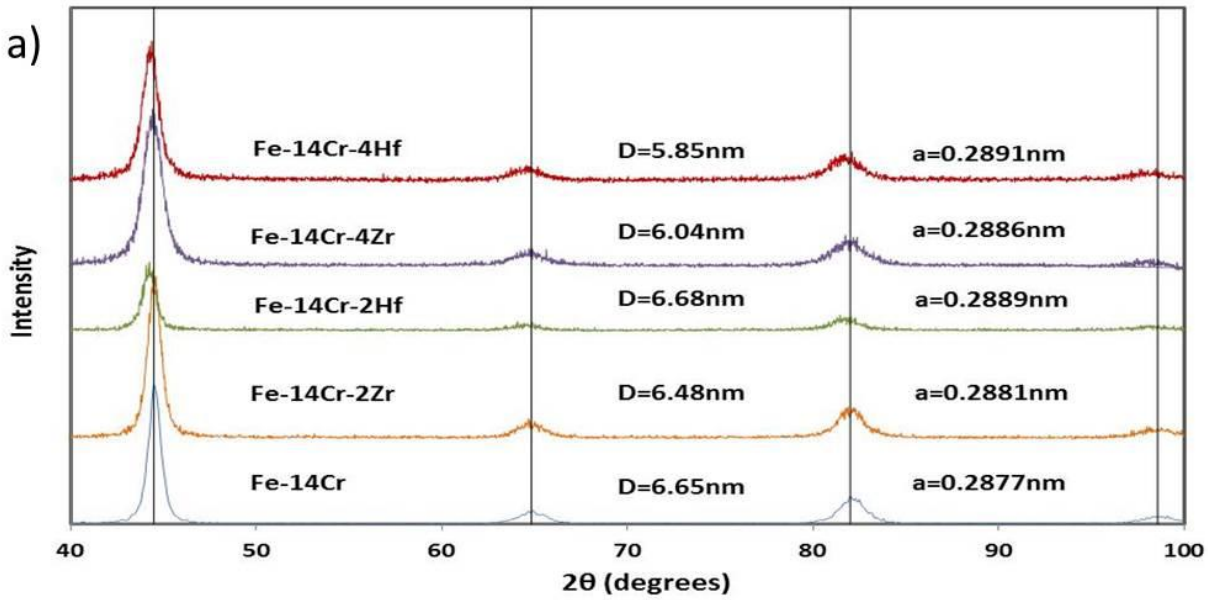
a)
Intensity
Fe-14Cr-4Hf
D=5.85nm
a=0.2891nm
Fe-14Cr-4Zr
D=6.04nm
a=0.2886nm
Fe-14Cr-2Hf
D=6.68nm
a=0.2889nm
Fe-14Cr-2Zr
D=6.48nm
a=0.2881nm
Fe-14Cr
D=6.65nm
a=0.2877nm
40
50
60
70
80
90
100
2θ (degrees)

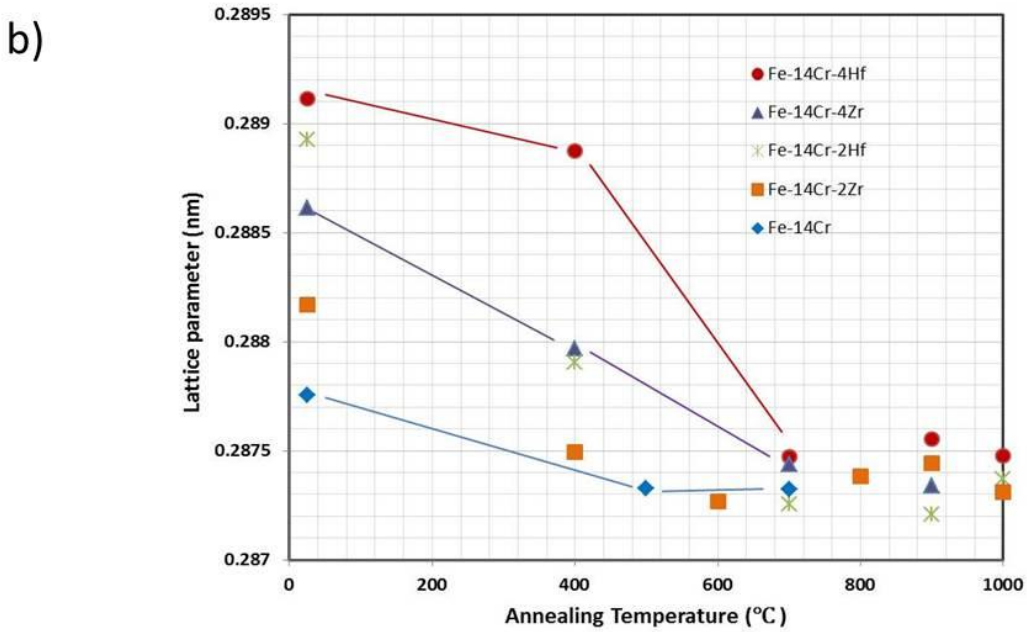
b)
0.2895
0.289
0.2885
0.288
0.2875
0.287
Lattice parameter (nm)
Fe-14Cr-4Hf
Fe-14Cr-4Zr
Fe-14Cr-2Hf
Fe-14Cr-2Zr
Fe-14Cr
0
200
400
600
800
1000
Annealing Temperature (℃)

Fig.2

a)

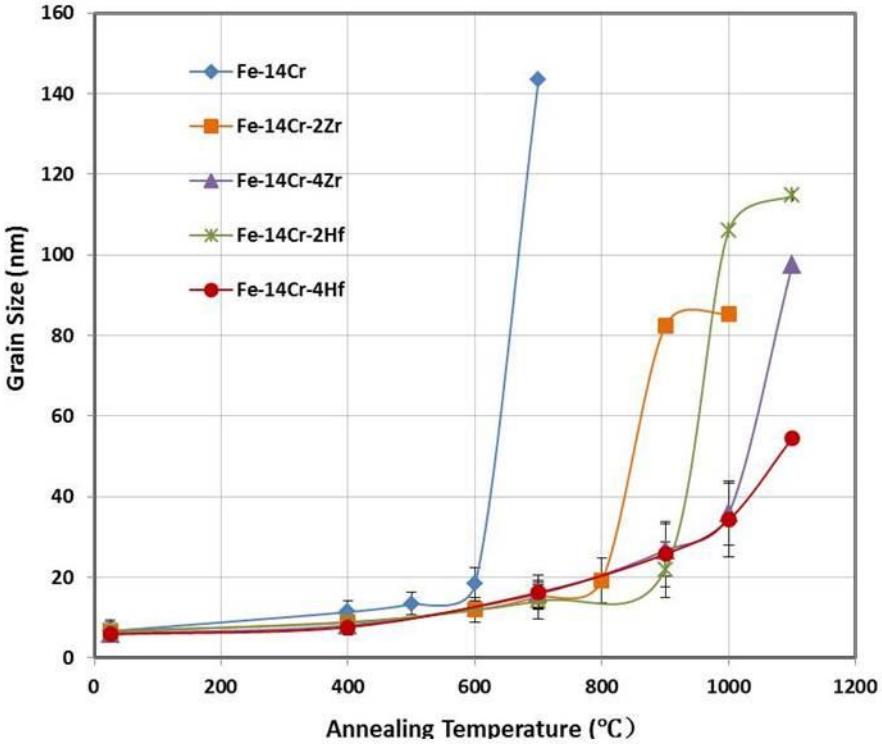
Grain Size (nm)
Annealing Temperature (℃)
Fe-14Cr
Fe-14Cr-2Zr
Fe-14Cr-4Zr
Fe-14Cr-2Hf
Fe-14Cr-4Hf

b)

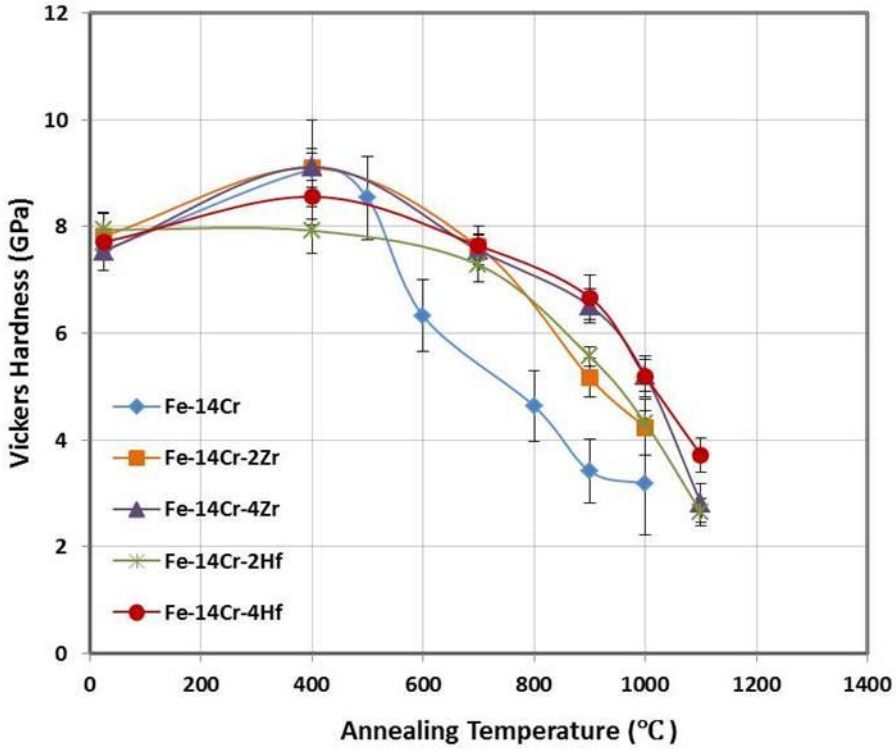
Vickers Hardness (GPa)
Annealing Temperature (℃)
Fe-14Cr
Fe-14Cr-2Zr
Fe-14Cr-4Zr
Fe-14Cr-2Hf
Fe-14Cr-4Hf

Fig.3

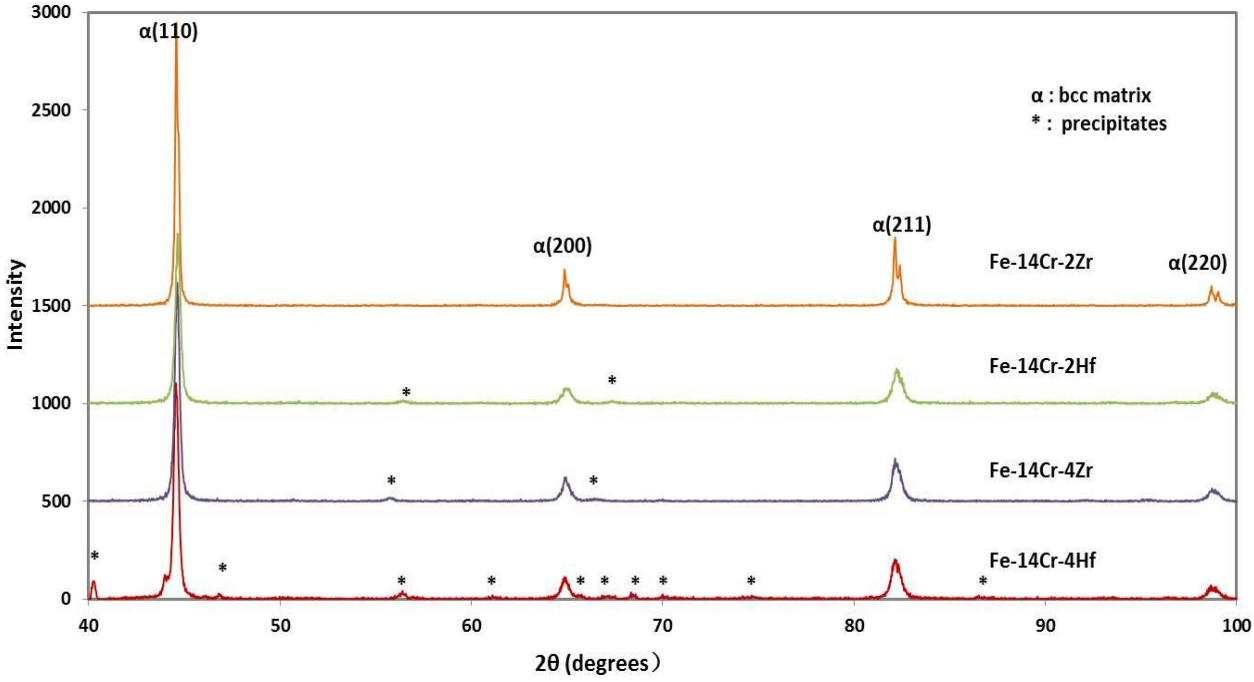
α(110)
α(200)
α(211)
α(220)
α : bcc matrix
* : precipitates
Fe-14Cr-2Zr
Fe-14Cr-2Hf
Fe-14Cr-4Zr
Fe-14Cr-4Hf
Intensity
2θ (degrees)
3000
2500
2000
1500
1000
500
0
40
50
60
70
80
90
100

Fig.4

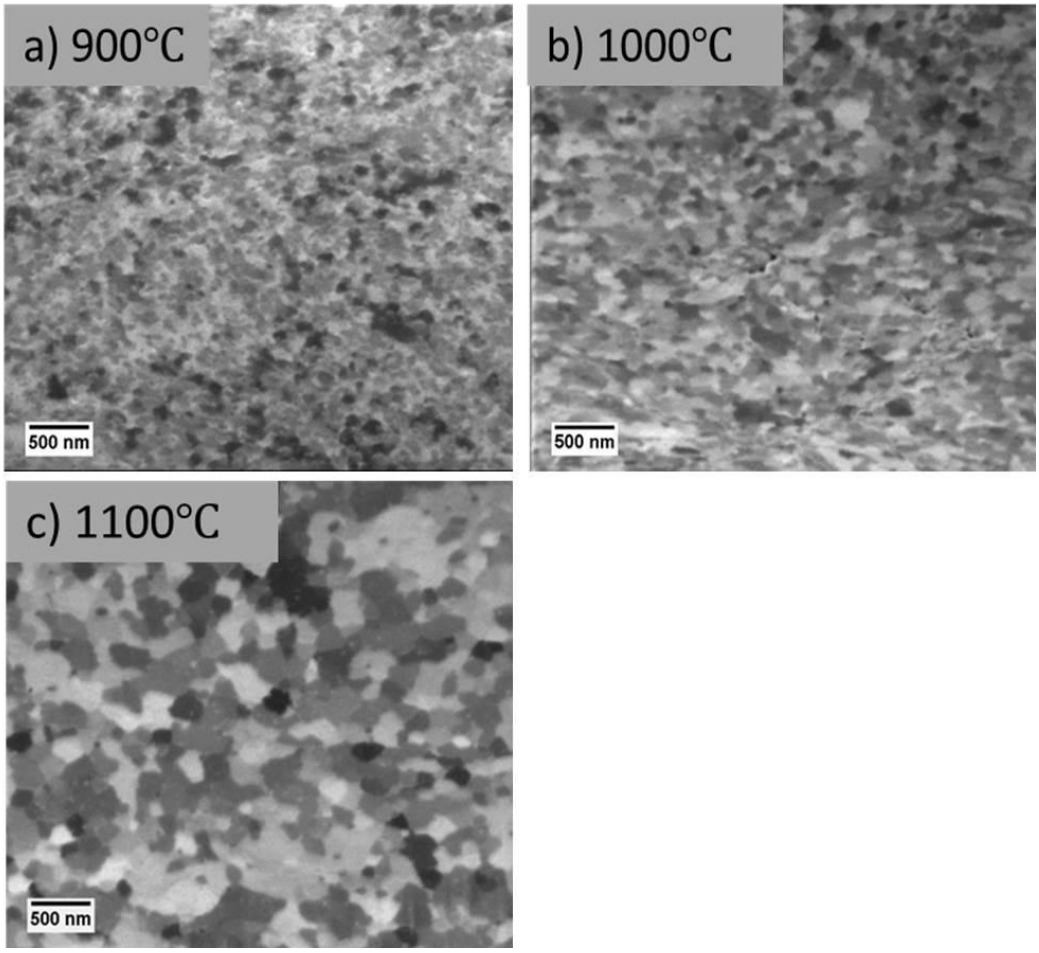

Fig.5

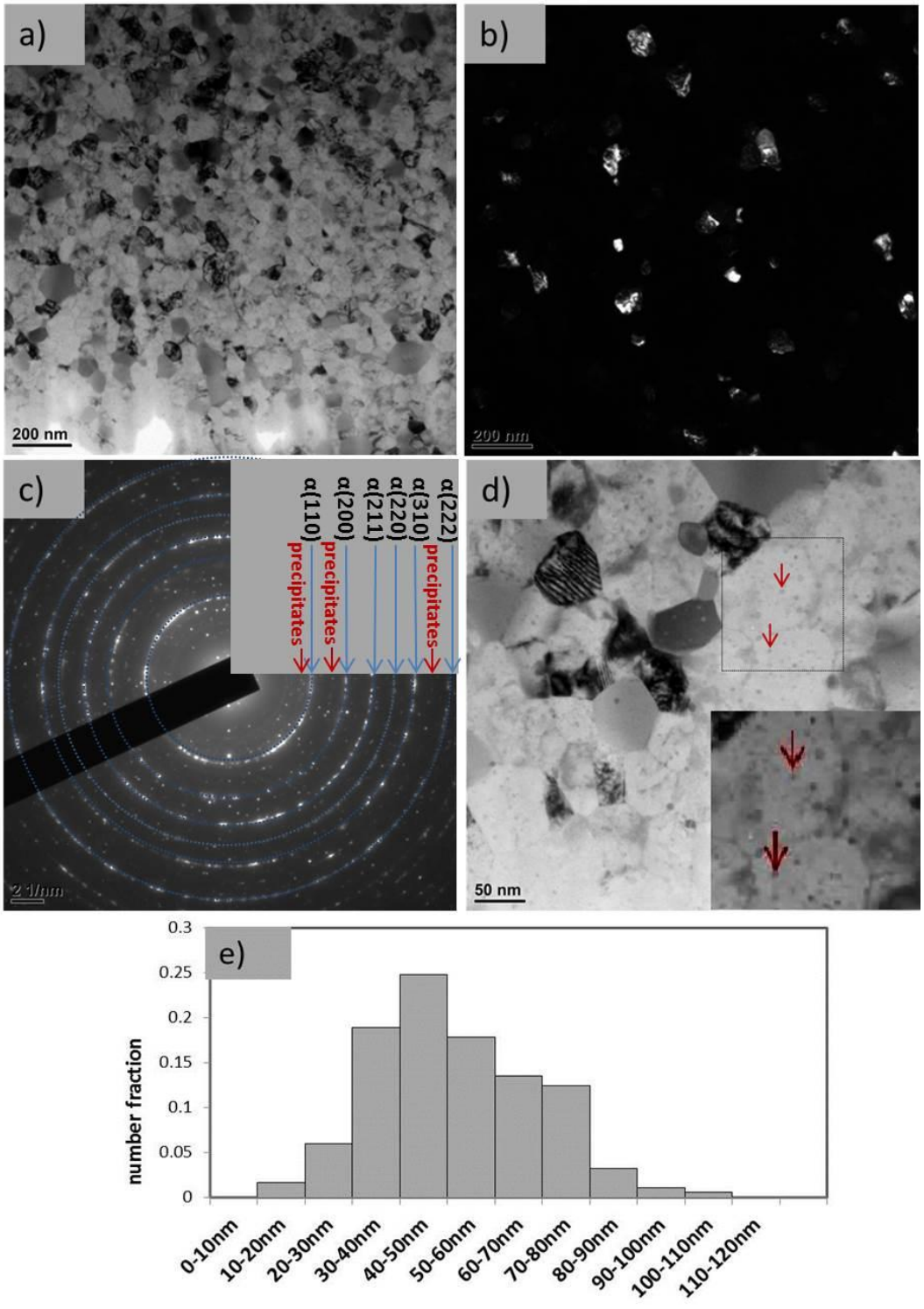
a)
200 nm
b)
200 nm
c)
α(110)
α(200)
α(211)
α(220)
α(310)
α(222)
precipitates
precipitates
precipitates
d)
50 nm
e)
number fraction
0.3
0.25
0.2
0.15
0.1
0.05
0
0-10nm
10-20nm
20-30nm
30-40nm
40-50nm
50-60nm
60-70nm
70-80nm
80-90nm
90-100nm
100-110nm
110-120nm

Fig.6

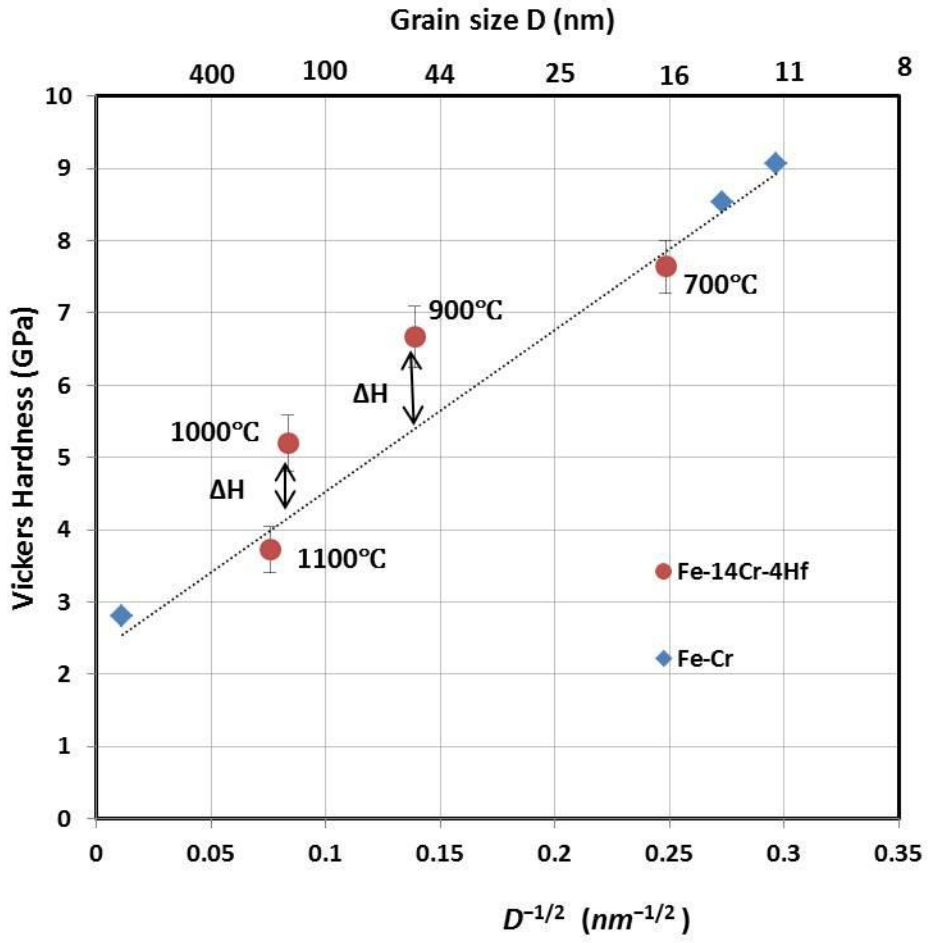
Grain size D (nm)
400
100
44
25
16
11
8
Vickers Hardness (GPa)
0
1
2
3
4
5
6
7
8
9
10
0
0.05
0.1
0.15
0.2
0.25
0.3
0.35
$D^{-1/2}$ ($nm^{-1/2}$)
700℃
900℃
1000℃
1100℃
ΔH
ΔH
Fe-14Cr-4Hf
Fe-Cr

Fig.7

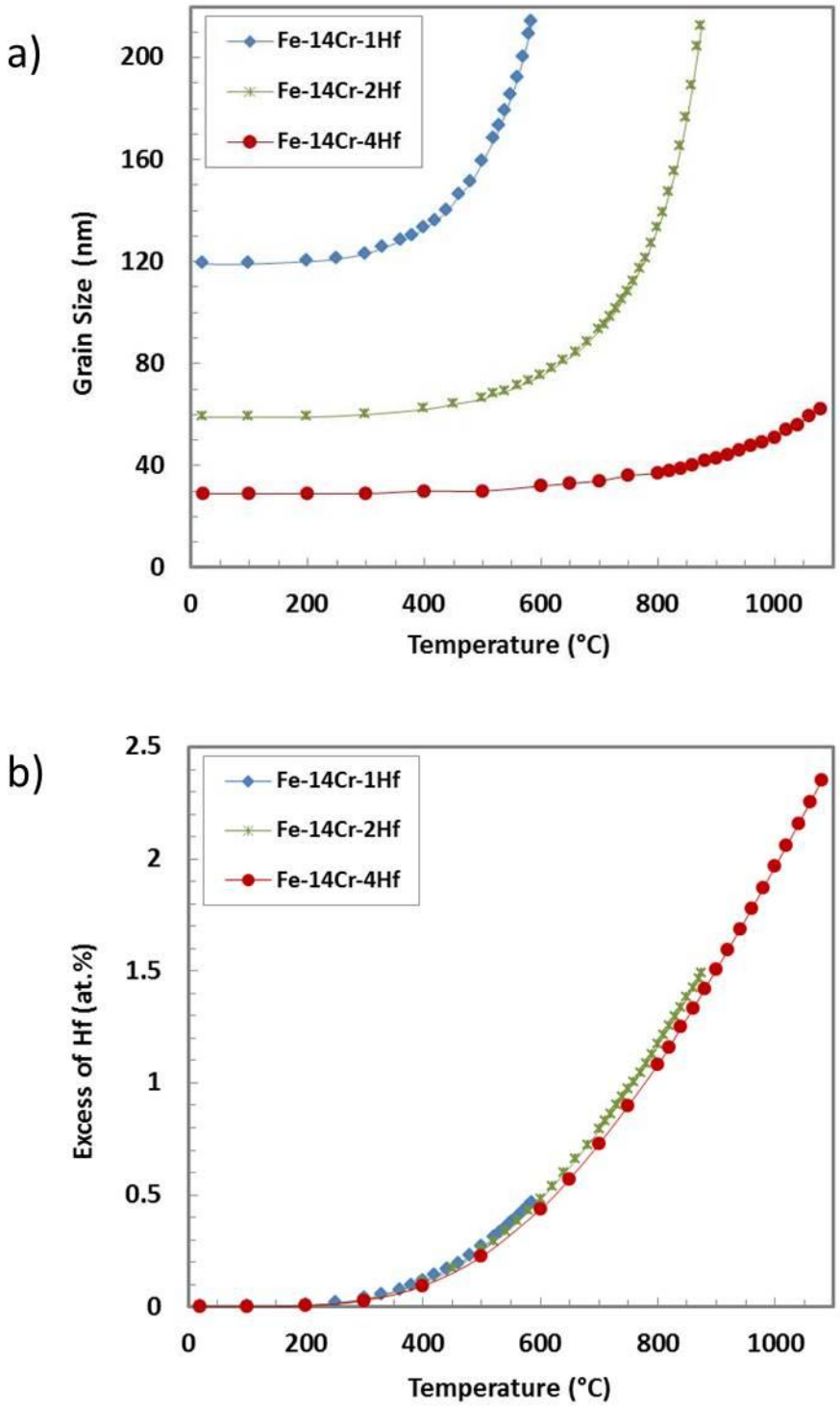
a)
Fe-14Cr-1Hf
Fe-14Cr-2Hf
Fe-14Cr-4Hf
Grain Size (nm)
0
40
80
120
160
200
0
200
400
600
800
1000
Temperature (°C)
b)
Fe-14Cr-1Hf
Fe-14Cr-2Hf
Fe-14Cr-4Hf
Excess of Hf (at.%)
0
0.5
1
1.5
2
2.5
0
200
400
600
800
1000
Temperature (°C)